ELSEVIER

International Journal of Heat and Fluid Flow 23 (2002) 627–638

International Journal of HEAT AND FLUID FLOW

www.elsevier.com/locate/ijhff

Numerical simulation method to resolve interactions between bubbles and turbulence

Takafumi Kawamura [a,*], Yoshiaki Kodama [b]

[a] *Department of Environmental & Ocean Engineering, Graduate School of Engineering, University of Tokyo, 7-3-1 Hongo Bunkyo-ku, Tokyo 113-8656, Japan*

[b] *Ship Performance Division, National Maritime Research Institute, 6-38-1 Shinkawa, Mitaka, Tokyo 181, Japan*

Abstract

A new computational method for investigating interactions between bubbles and turbulence has been developed. Both liquid and gas phases are treated as incompressible fluids and solved by a finite volume method, while the interface between the phases is resolved by a front-tracking method. The accuracy validation carried out for a problem of a single rising bubble has shown this method is capable of simulating flow around deformed bubbles with relatively small number of grid points. Then the method was applied to a direct numerical simulation of a fully developed turbulent channel flow containing bubbles. Statistics of the friction coefficient and the modulation of turbulence intensity were obtained, and they were in qualitative agreement with experiments. © 2002 Elsevier Science Inc. All rights reserved.

Keywords: Direct numerical simulation; Bubble flow; Multiphase flow; Turbulence modulation; Frictional drag

1. Introduction

Bubbly flows appear in many engineering and environmental applications. Understanding the characteristics of bubbly flows is important for the design of multi-fluid systems or estimating the mass transfer rate between the atmosphere and the ocean. Bubbly flows involve wide range of scales from bubble diameter to macroscopic flow, and the interactions between those scales make the physics of bubbly flows more complex than that of single phase flows.

There are three ways to simulate bubbly flows numerically. The three numerical simulation methods differ in the scale range that is explicitly solved. The first way is to solve phase-averaged equations of fluid, in which the macroscopic effect of interactions between phases is modeled by semi-empirical constitutive equations (Drew, 1983). The second way is to model the dispersed phase by point force distributions at discrete location of dispersed phase (bubbles or solid particles). In this method, the scale of distances between bubbles or particles is explicitly solved, but the scale of bubble or particle size must still be modeled by semi-empirical equations (Elghobashi and Truesdell, 1992). The third way is to simulate flows directly by implementing physical boundary conditions at the interface between the phases. Although the computational load is highest, only this method can resolve the full interactions between two phases. Numerical methods of this type have been applied mostly to flows around a single bubble or particles (Ryskin and Leal, 1984; Takagi and Matsumoto, 1995). However, the recent increase in the computer power has made it possible to apply this method to more complex bubbly flows. Kajishima et al. (2001) have studied particle-laden turbulent channel flow using a direct numerical simulation (DNS) method for solid particles. Sugiyama et al. (2001) investigated bubbly flows using a similar method, in which bubbles keep spherical shape, while Kanai and Miyata (2001) carried out a DNS of turbulent Couette flow containing deformable bubbles by use of the marker density method.

One application of bubbles in which we are particularly interested is reduction of the frictional drag of a turbulent boundary layer. Many experiments (Madavan et al., 1985; Guin et al., 1996; Takahashi et al., 1997) confirmed the reduction of the frictional drag, but the detailed mechanism how bubbles reduce frictional drag has not been well understood. This is partially due to the

* Corresponding author. Fax: +81-3-3815-8360.

E-mail addresses: kawamura@fluidlab.naoe.t.u-tokyo.ac.jp (T. Kawamura), kodama@nmri.go.jp (Y. Kodama).

0142-727X/02/$ - see front matter © 2002 Elsevier Science Inc. All rights reserved.
PII: S0142-727X(02)00158-3

Nomenclature

A_{nm}, B_{nm}	coefficients used in the spherical harmonics
C_D	drag coefficient
C_f	normalized friction coefficient $= \tau_w/\tau_{w0}$
D	bubble diameter
D^+	bubble diameter in viscous unit $= Du_\tau H/\nu$
Fr	Froude number $= U_m/\sqrt{gD}$
H	half width of the channel
N_B	number of bubbles
P_{nm}	Legendre associate polynomial
p	static pressure
Q	second invariant of the velocity gradient tensor
r	bubble radius
Re_τ	Reynolds number $= u_\tau H/\nu$
We	Weber number $= \rho U_m^2 D/\sigma$
t	time
t^+	nondimensional time in viscous unit $= u_\tau^2 t/\nu$
u_i	velocity vector
U_m	mean velocity
u_τ	friction velocity $= \sqrt{\tau_w/\rho}$
x_i	Cartesian coordinate
Greeks	
α	mean void ratio
ν	kinematic viscosity
ρ	fluid density
σ	surface tension
τ_w	shear stress at the wall
τ_{w0}	shear stress at the wall without bubbles

experimental difficulties. Detailed information of the flow is missing, because the dense suspension of bubbles strongly hinders measurements of the flow by LDV or PIV. It is also very difficult to control experimental conditions. Kato et al. (1999) showed that the size of bubbles generated by injecting air through a hole on the wall depends more on the wall shear stress than on the size of the hole. This fact makes it difficult to control the Reynolds number and the bubble size independently. It is also difficult to control the other parameters involved in bubbly flows such as Weber number or Froude number.

The ultimate goal of this study is to develop a numerical simulation method for solving these problems. Especially we hope that numerical simulations elucidate the interactions between bubbles and turbulent boundary layer. Fig. 1 shows a snap photo of the flow dealt with in this study. It is noted that the size of bubbles is relatively large, and the effect of the deformation of bubbles is supposed to be significant. In order to investigate the interaction between turbulence and bubbles of this size, DNS methods which simultaneously resolve turbulence and bubbles are useful. The number of grid points for performing DNS depends on the ratio of the bubble size to the boundary layer boundary layer thickness, and on the number of points required for resolving a bubble. Therefore we developed a new front-tracking method, which is capable of modeling deformable bubbles with small number of grid points.

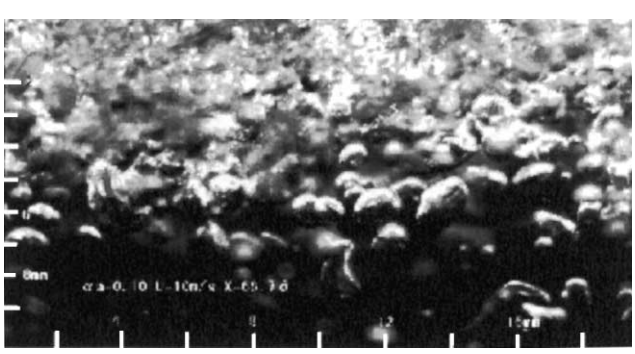

Fig. 1. Photograph of bubbles in a turbulent channel flow (Takahashi et al., 1997).

The following sections of this paper provide a description of the numerical method, a validation of the method for a single rising bubble, and a preliminary application to a turbulent bubbly channel flow at a low Reynolds number.

2. Numerical method

2.1. Governing equations

Both water and air phases are treated as incompressible fluids, and the continuity of stress is implemented at the interface. The governing equations for each phase are the Navier–Stokes equation,

$$\frac{\partial u_i}{\partial t} = -\frac{\partial u_i u_j}{\partial x_j} + \frac{\partial}{\partial x_j}\left\{\nu\left(\frac{\partial u_i}{x_j} + \frac{\partial u_j}{x_i}\right)\right\} - \frac{1}{\rho}\frac{\partial p}{\partial x_i} \tag{1}$$

and the continuity equation

$$\frac{\partial u_i}{\partial x_i} = 0 \tag{2}$$

where x_i, u_i, and p are the Cartesian coordinate, the velocity components, and static pressure respectively. The fluid density ρ and the kinematic viscosity ν take values of either water or air depending on whether the center of the computational cell belongs to water or air.

2.2. Interface tracking method

There are several methods for expressing the moving interface between two fluids, such as the VOF method (Hirt and Nichols, 1981), the level-set method (Osher and Sethian, 1998), and the front-tracking method (Unverdi and Tryggvason, 1992). The VOF and level-set methods are categorized as the front capturing methods which track the movement of volume and find the interface in an indirect way. One of the merits of the front capturing methods is that collision and breakup of interfaces are easily treated. On the other hand, the front-tracking method tracks the interface directly allowing more accurate calculation of the curvature of the interface, although treatment of surface re-structuring is complicated. We use the front-tracking method, since accurate calculation of the interface curvature is very important for the flows investigated in this study.

Each bubble is expressed by its center position and radius distribution around the center as shown in Fig. 2. Marker particles are placed on each bubble regularly on a two-dimensional spherical grid (θ, ϕ). In the beginning of each time step, the positions of the marker particles are updated using the velocity interpolated from the rectangular grid for solving the Navier–Stokes equations. After the marker particles are moved, the position of the center is updated. Then the radius at each point $r(\theta, \phi)$ around the new center is calculated and expanded in a series of spherical harmonic function,

$$r(\theta, \phi) = \sum_{n=0}^{N} \sum_{m=0}^{n} P_{nm}(\cos\theta)\{A_{nm}\cos m\phi + B_{nm}\sin m\phi\} \tag{3}$$

in which N is the number of the deformation modes considered, P_{nm} is Legendre associate polynomial. N is set to 8 in this study. The coefficients A_{nm} and B_{nm} are obtained by numerical integrations.

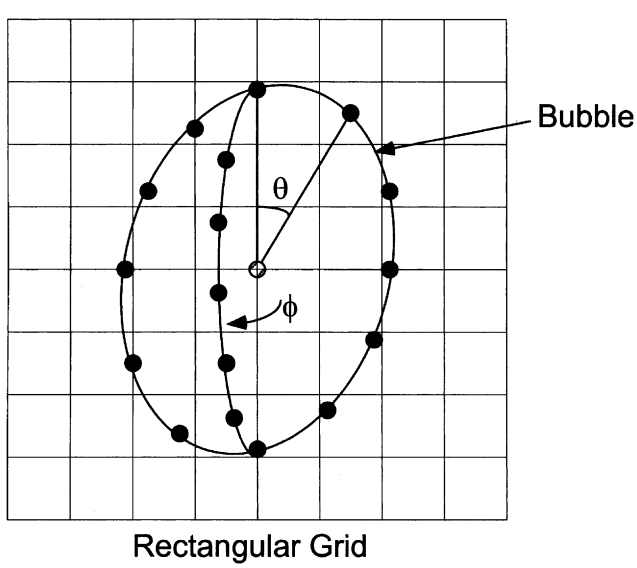

Fig. 2. Schematic sketch of the front-tracking method.

The primary merit of this merit is that the curvature of the interface is accurately computed with relatively small number of grid points. Another advantage is that deformations of high wave number modes, which give rise to numerical instabilities, can be filtered out. Whereas the shortcomings are that the radius must be a single-valued function of θ and ϕ. Therefore, this method cannot deal with deformations beyond a certain limit, collision or separation of bubbles.

Since the compressibility of air is neglected, the volume of the bubble must be constant. The value of the coefficient A_{00} is adjusted in the reconstruction procedure of the bubble shape so that the volume of the bubble is kept at the initial value.

2.3. Solution algorithm

A second-order finite volume method is used for the spatial discretization on a rectangular grid system fixed to the space, and a second-order semi-implicit fractional step method is used for the time integration. At the beginning of each time step, the positions and shapes of bubbles are determined, and the values of density and the kinematic viscosity in each cell are set to values of water or air. Whether a cell-center point is inside a bubble or not is judged from Eq. (3). Then the dynamic boundary condition is set in cells containing interfaces. The surface tension is treated as a pressure jump across the interface. The curvature of the interface is calculated from Eq. (3) analytically. Using this interface boundary condition the momentum equations (1) are semi-implicitly integrated, and then corrected by solving a Poisson equation for the pressure. The Poisson equation for the pressure is solved by a multigrid method.

3. Single rising bubble

The accuracy of the computational method was examined for the problem of a single bubble rising in quiescent water. Computations were carried out using maximum of $64 \times 64 \times 64$ cells for a maximum domain size of 16 diameters cube. A spherical bubble is initially placed at the center of the computational domain. The computational domain is moved at the velocity of the center of the volume of the bubble. The velocity of the center is calculated using the history of the positions at previous 20 steps. A fixed frame of reference is used for defining the velocity vector of the fluids, and the movement of the grid is considered in computing the convective terms of the momentum equation by modifying the volume flux through cell faces. The top face of the computational domain is treated as an inflow boundary, and the other five faces are treated as outflow

boundaries. At the inflow boundary, the velocity is kept at zero, and a homogeneous Neumann condition is applied to the pressure. At the outflow boundaries, the velocity is linearly extrapolated, and the pressure is kept at a reference pressure level. In the following presentation of the results for a single rising bubble, the length and the velocity scales are nondimensionalized with respect to the bubble diameter and the mean rising speed of the bubble respectively. The z-axis is taken in the vertical direction, while x and y-axes are taken in the horizontal directions.

The results are examined focusing on the drag coefficient C_D obtained from the terminal rising velocity. The influences of the three computational parameters, the size of the computational domain, the number of grid points per bubble diameter, and the number of deformation modes are examined. The bubble diameter of 2 mm, the domain size of 8 diameters cube, $N = 6$, 10 grid points per bubble diameter, were used as the standard condition, and influence of each parameter was investigated by varying one parameter with the other parameter being fixed.

Fig. 3 shows that the influence of the domain size is small when it is larger than 8 diameters. It was observed that the development of the velocity field around the bubble was hampered when the size of the computational domain was not sufficiently large. As a result, the rising speed was small and the drag coefficient was large.

The influence of the number of deformation modes (N in Eq. (3)) is shown in Fig. 4. The precision of the expression of the bubble shape depends on the number of deformation modes considered. Accordingly, the drag coefficient is also influenced by this parameter. The final shape of the bubble of $D = 2$ mm is almost ellipsoidal, and the ratio between the long and short axes is about 1.5, which is in good agreement with the experimental observation by Kubota et al. (1967). Fig. 4 shows that the drag coefficient almost convergences at $N = 6$ for the bubble of this size.

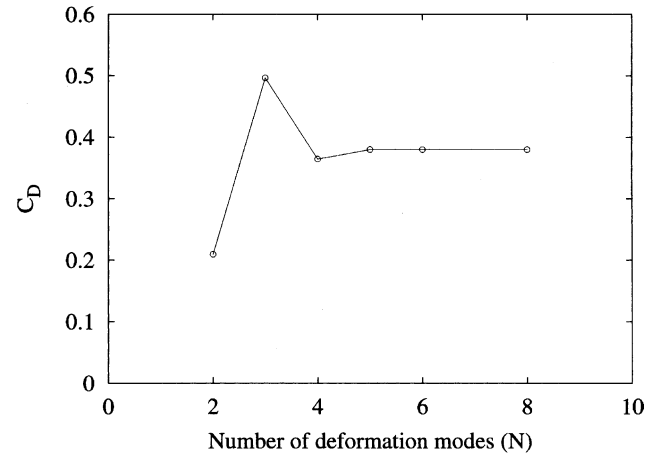

Fig. 4. Drag coefficient of a single rising bubble in clean water versus the number of deformation modes.

Fig. 5 shows the influence of the number of the grid points per bubble diameter. It is shown that from eight to ten grid points per bubble diameter are required for the drag coefficient to converge. This result is consistent with Takiguchi et al. (1998), who reported that the required number was from five to ten for a computation of flow around a spherical solid particle using a rectangular grid.

Fig. 6 shows the comparison of the computed drag coefficient using the previously mentioned standard conditions versus the bubble diameter and an empirical formula proposed by Tomiyama et al. (1995). A bubble of $D = 1$ mm or smaller is almost spherical and rises straight up, while a larger bubble is deformed and shows nonaxisymmetric swing motions. Computations reproduce this behavior well, and the calculated values of C_D are in good agreement with the empirical formula.

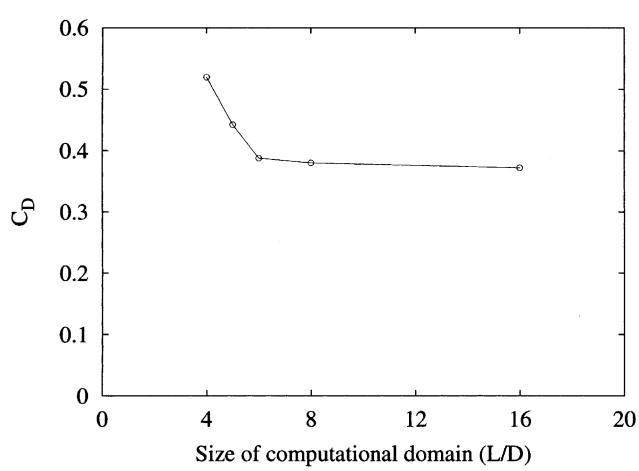

Fig. 3. Drag coefficient of a single rising bubble in clean water versus domain size.

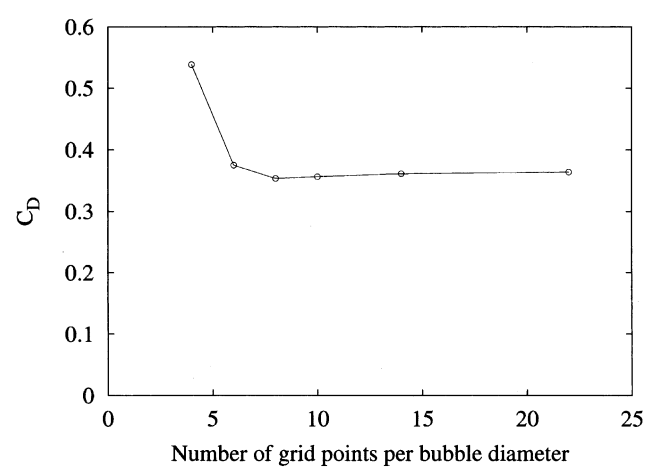

Fig. 5. Drag coefficient of a single rising bubble in clean water versus number of grid points per diameter.

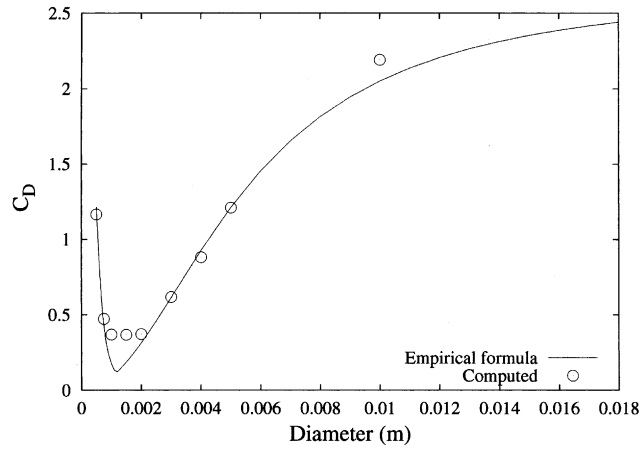

Fig. 6. Drag coefficient of a single rising bubble in clean water versus diameter.

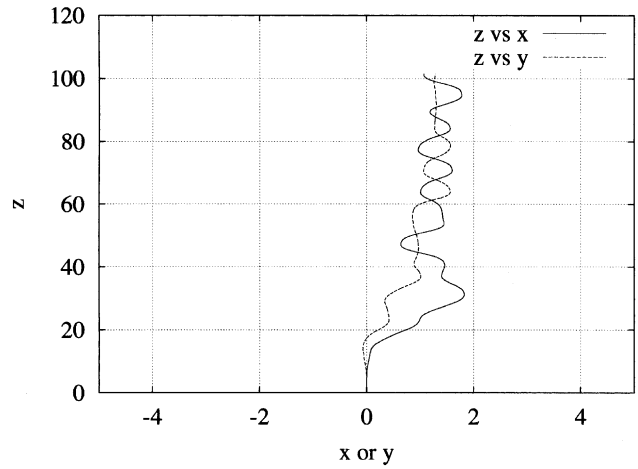

Fig. 8. Time evolution of the center position of a rising bubble of $D = 3$ mm.

Fig. 7 shows computed ellipsoidal shape of the bubble for two diameters $D = 1$ and 3 mm. The flow and the shape of the bubbles are axisymmetric and steady at $D = 1$ mm, while at $D = 3$ mm nonaxisymmetric and unsteady vortex shedding is observed. The time evolution of the bubble-center position from the starting point for a bubble of $D = 3$ mm shown in Fig. 8 indicates a plane zigzag motion of the bubble. The direction of the oscillation changes, suggesting that this motion is not very stable. The wave length of the zigzag motion was estimated to be about 16 diameters, which is close to the experimental observation by Ellingsen and Risso (2001) for $D = 2.5$ mm. Fig. 9 shows the relation between the lateral displacement and the inclination of the bubble for $D = 3$ mm. The relation agrees with the experiment by Ellingsen and Risso (2001). The three dimensional structure of the wake is illustrated in Fig. 10. The wake structure from the bubble is characterized by a sequence of vortex loops, and it is very similar to that near a solid sphere described, for example, by Achenbach (1974). The vortex shedding and the zigzag motion are synchronized, and the computed Strouhal number based on the diameter and the mean rising velocity is 0.07. This is in good agreement with the experiment by Ellingsen and Risso (2001). This Strouhal number is about half of that for a solid sphere supported in a uniform flow at the same Reynolds number of 750 (Achenbach, 1974). This is due to deformation of the bubble and the difference in the boundary condition on the surface.

4. DNS of a bubbly turbulent channel flow

4.1. Condition of computations

A fully developed turbulent channel flow containing bubbles was investigated by the present numerical

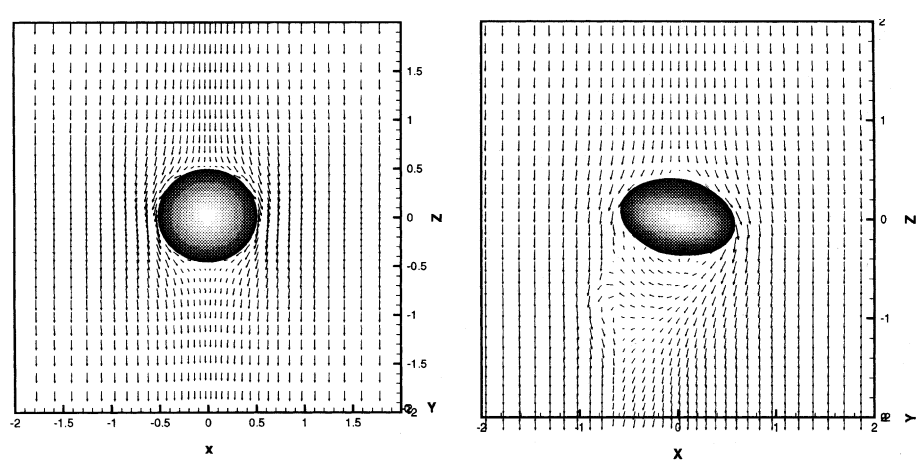

(a) D = 1 mm (b) D = 3 mm

Fig. 7. Computed shape of the bubble rising in clean water. The vectors show an instantaneous velocity field on the plane containing the center of the bubble. The velocity is relative to the coordinate system moving with the center of the bubble. Velocity vectors at every second grid point are shown. (a) $D = 1$ mm and (b) $D = 3$ mm.

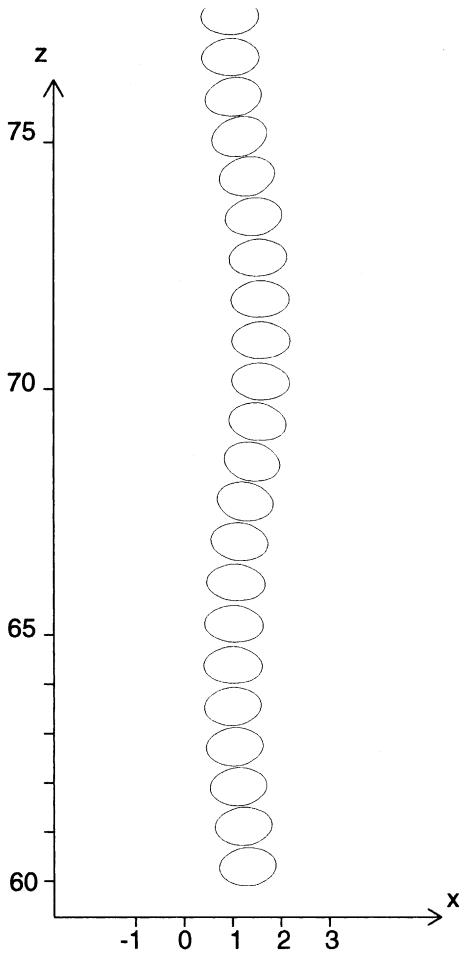

Fig. 9. Time evolution of the bubble shape and position projected on the x–z plane for a rising bubble of $D = 3$ mm.

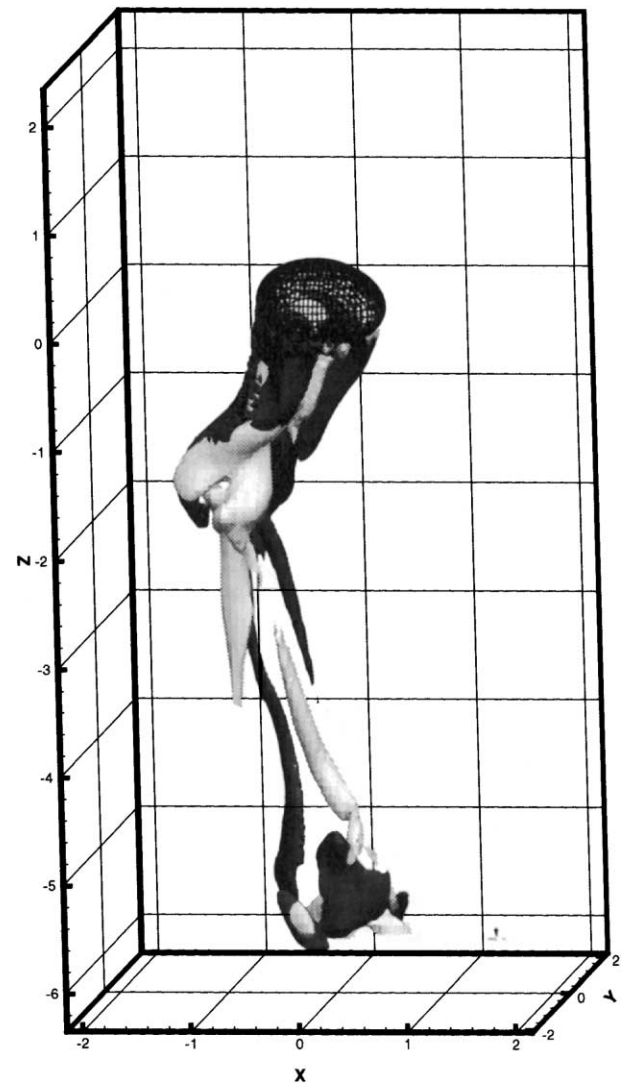

Fig. 10. Iso-surfaces of the longitudinal component of the vorticity $\omega_3 = \pm 2$ for a rising bubble of $D = 3$ mm. The dark and light surfaces indicate positive (counter clockwise rotation when seen from the top) and negative vorticity, respectively. The bubble surface is shown by wire frames.

method. Before introducing the bubbles, a fully developed single-phase turbulent channel flow at the Reynolds number $Re_\tau = 180$, based on the friction velocity u_τ and a half width of the channel H, was computed. The size of the computational domain was set to $6.4H \times 2H \times 3.2H$, in the streamwise, wall-normal and spanwise directions respectively. A periodic boundary condition was used in the streamwise and spanwise directions. The x-, y- and z-axes are taken in the streamwise, wall-normal and spanwise directions respectively. The number of the grid points is $64 \times 64 \times 64$. The profiles of computed mean velocity and turbulence intensity agree well with the DNS results of Kim et al. (1986) as shown in Fig. 11.

A total of eight DNS runs are performed for investigating the influences of the parameters such as the void ratio, the bubble size, buoyancy, and surface tension on the drag reduction. The parameters are summarized in Table 1. With the presently available computer resources, the Reynolds number at which DNS computations can be performed is limited to the order of $Re_\tau = 100$, which is at least an order of magnitude smaller than in the experiment by Takahashi et al. (1997). One way to achieve higher Reynolds number in the computation is to perform large eddy simulation by introducing a subgrid scale model. However, since this is the first application of the present numerical method to a turbulent flow, subgrid scale models are not used in order to avoid uncertainty and complexity. On the other hand, the other parameters such as the Weber number, or the Froude number are on the same order as the experiment.

At the beginning of the computation (nondimensional time $t^+ = u_\tau^2/\nu = 0$), the velocity field was initialized by an instantaneous velocity field of the single phase flow and bubbles were introduced at the same time. When the number of bubbles in the periodic computational domain was 54, bubbles were initially

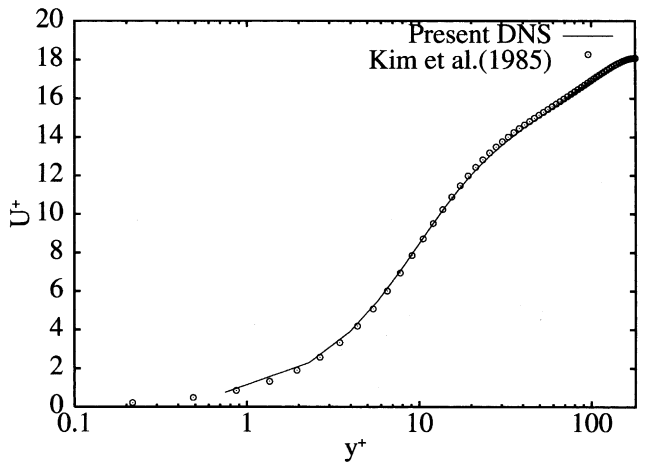

(a) Mean velocity

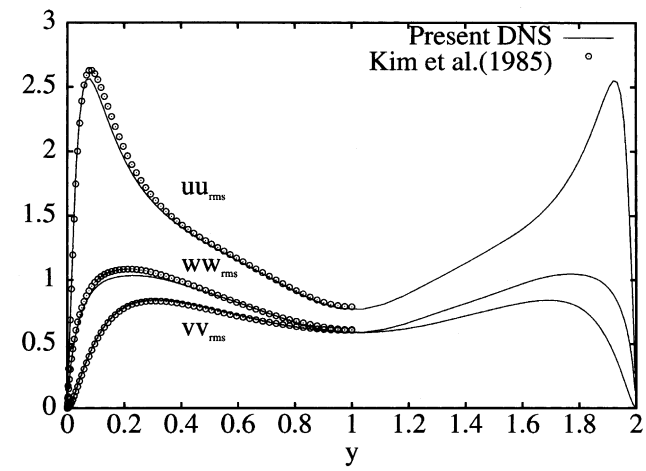

(b) Turbulence intensities

Fig. 11. DNS of single phase turbulent channel flow: (a) mean velocity and (b) turbulence intensities.

Table 1
Condition of computation for DNS of fully developed turbulent channel flow

Run	We	$1/Fr^2$	D^+	N_B	α (%)	C_f
0	–	0	–	–	0.0	1.0
1	9.2	0	90	54	8.6	1.23
2	37.0	0	90	54	8.6	1.16
3	9.2	0	90	18	2.9	1.12
4	37.0	0	90	18	2.9	1.12
5	9.2	6.8×10^3	90	18	2.9	1.11
6	7.3	0	71.4	36	2.9	1.15
7	7.3	5.4×10^3	71.4	36	2.9	1.12
8	11.6	0	113	9	2.9	1.10

placed on the grid of $6 \times 3 \times 3$ in the streamwise, wall-normal, and spanwise directions respectively. Grids of $3 \times 3 \times 4$, $3 \times 2 \times 2$, and $3 \times 3 \times 1$ were used for the initial locations for computations with 36, 18 and 9 bubbles respectively. An example of the initial distribution of bubbles is shown in Fig. 12. The influence of the initial distribution of bubbles disappeared before

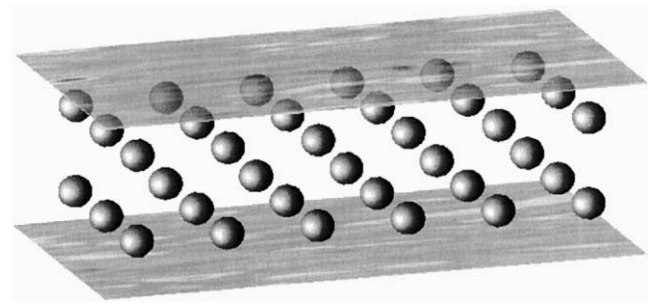

Fig. 12. Initial distribution of bubbles at $t^+ = 0$ in the DNS Run-1 and 2 of the bubbly channel flow.

$t^+ = 100$, as the bubbles were stirred by the turbulence in the liquid phase. At the beginning of the computation, the bubbles suddenly appeared as if the water in the spherical regions suddenly turned into air without influencing the velocity field. This unnatural situation causes oscillation of bubble shapes. However, this oscillation was quickly damped by the viscous effect and vanished before $t^+ = 10$.

The mean pressure gradient was automatically adjusted so that the volume flow rate was kept constant. The computational domain is periodic in the streamwise and spanwise directions for both phases. When a bubble passes through a periodic boundary, the bubble is cut into two pieces (or four at the corner), and they are computed at the both sides of the periodic boundary.

The same computational domain, and the same number of grid points as the single phase flow computation were used. The grid requirements to resolve bubbles restrict the size of bubbles which can be computed in the same framework as the boundary layer flow. As summarized in Table 1, the bubble diameter in the computations ranged between 0.40 and 0.63 H. The number of grid points in the streamwise direction, in which the grid spacing was the largest, was from four to six, while in the spanwise and wall-normal directions the number was twice or more. This resolution is close to the minimum required resolution for a single rising bubble as investigated in the previous section. However, since the relative velocity between bubbles and surrounding fluid is much smaller in the channel flow than in the case of a rising bubble, this resolution is supposed to be sufficient (Takiguchi et al., 1998).

The bubble size can be scaled by the boundary layer thickness and by the size of the wall-turbulence structure. The first one, D/H was between 0.40 and 0.63 in the present DNS, while this ratio was between 0.1 and 0.2 in the experiment. In this respect the bubble size is large in the present DNS computations, and it must be assumed that the results are influenced by this difference.

On the other hand, the bubble size in the viscous unit D^+ was between 71 and 113 in the present computations, while in the experiment D^+ was about 200. If we assume

the scale of wall-turbulence structure can be scaled by the viscous unit, the bubble size in the computation in this respect is small. Therefore, unfortunately, the following results cannot be directly compared with the experiment. The numerical results are used to discuss qualitative influences of the bubbles and the bubble related parameters on the turbulence and the frictional drag.

4.2. Results and discussion

It is supposed that the effect of bubbles on turbulent boundary layer can appear in two ways. One is interaction between bubbles and shear flow, which can also occur in a laminar shear flow. A bubble placed in a shear flow causes local flow to satisfy the stress free condition at the bubble surface. This results in additional dissipation, and its macroscopic influence can be expressed by the effective viscosity defined as

$$\mu_{\mathrm{eff}} = (1+\alpha)\mu_{\mathrm{L}} \tag{4}$$

in which μ_{L} is the viscosity of water. At a low Reynolds number, at which the laminar dissipation in the bulk flow has significant contribution, this additional laminar dissipation is supposed to increase the frictional drag. The second effect of bubbles is the modification of turbulence in the liquid phase. Gore and Crowe (1989) have shown solid particles in the carrier phase either increase or decrease the turbulence intensity depending on the ratio between the particle size and the characteristic length scale of turbulence. The influence of gas bubbles on turbulence of the carrier liquid phase has not been extensively studied yet. However, the recent experiment of a bubbly channel flow by Kato et al. (1999) suggested that the presence of bubbles suppressed the Reynolds stress and the intensity of streamwise fluctuation.

Fig. 13 shows the time histories of the normalized mean wall shear stress C_f for the DNS runs 0, 3 and 6. After the bubbles are introduced at $t^+ = 0$, the mean wall shear stress increases and reaches a steady level at $t^+ = 400$–800. The average values of C_f computed for 1000 viscous time units from $t^+ = 800$ are shown in the Table 1. Hereafter, time-average denotes an time-average from $t^+ = 800$ to 1800. It is noted that the frictional drag is increased in all cases unlike in the experiment. This is partially due to the increase in the effective viscosity, which dominates over the other effects of bubbles.

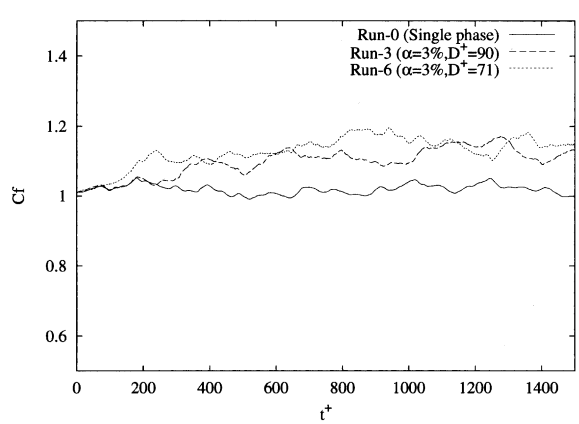

Fig. 13. Time history of the normalized friction coefficient in the DNS of the bubbly channel flow.

Fig. 14 shows the values of C_f versus four parameters α, D^+, Fr and We. The influence of the void ratio α for a fixed diameter and surface tension at zero gravitational acceleration is shown in Fig. 14(a). The value of C_f is increased as the void ratio α is increased, since the increase in the effective viscosity is proportional to the void ratio. Fig. 14(b) shows that C_f is decreased with increasing bubble diameter D^+ for a fixed void ratio $\alpha = 2.9\%$ at zero gravitational acceleration. As shown later, the increase in the turbulence intensity at the same void ratio is larger with smaller bubbles. Perhaps this is related to the increase in the frictional drag.

The influence of the gravitational acceleration in the direction normal to the walls decreases C_f as shown in Fig. 14(c) for two diameters at a fixed void ratio $\alpha = 2.9\%$. Snapshots of the distribution of bubbles at $t^+ = 1500$ for Run-6 and 7 shown in Fig. 15 and profiles of time-averaged void ratio for the same runs in Fig. 16 indicate that bubbles are concentrated toward the top wall to which the buoyancy force points. This concentration of bubbles is supposed to suppress turbulent momentum transport in the wall-normal direction. Fig. 14(d) shows that effect of the surface tension on C_f is negligible, although the deformation of bubbles is very different as shown in Fig. 17. The effect of bubble size on the reduction of skin friction is one of the major issues that have not been addressed in previous experimental studies, altough it is practically very important. However, the recent experimental study by Takahashi et al. (2001) has shown that the drag reduction rate has a positive correlation with the size of bubbles. When the bubble size is increased, the ratio of the bubble size to the scale of turbulence or to the boundary layer thickness increases proportionally. At the same time, the effect of buoyancy relatively increases, and the effect of surface tension decreases. The present numerical results suggest that the relative increase in buoyancy and the size ratio may have positive effect on the drag reduction.

Fig. 18 shows profiles of the turbulence intensity components for the DNS Run-0, 1, 3, 6 and 8. The influence of the void ratio is compared in the left column of three figures, and that of the bubble diameter is compared in the right column. In all the cases with bubbles the wall-normal and spanwise components are increased, the influence on the streamwise component is not as clear as that for the other two components. However, the streamwise component is decreased in the

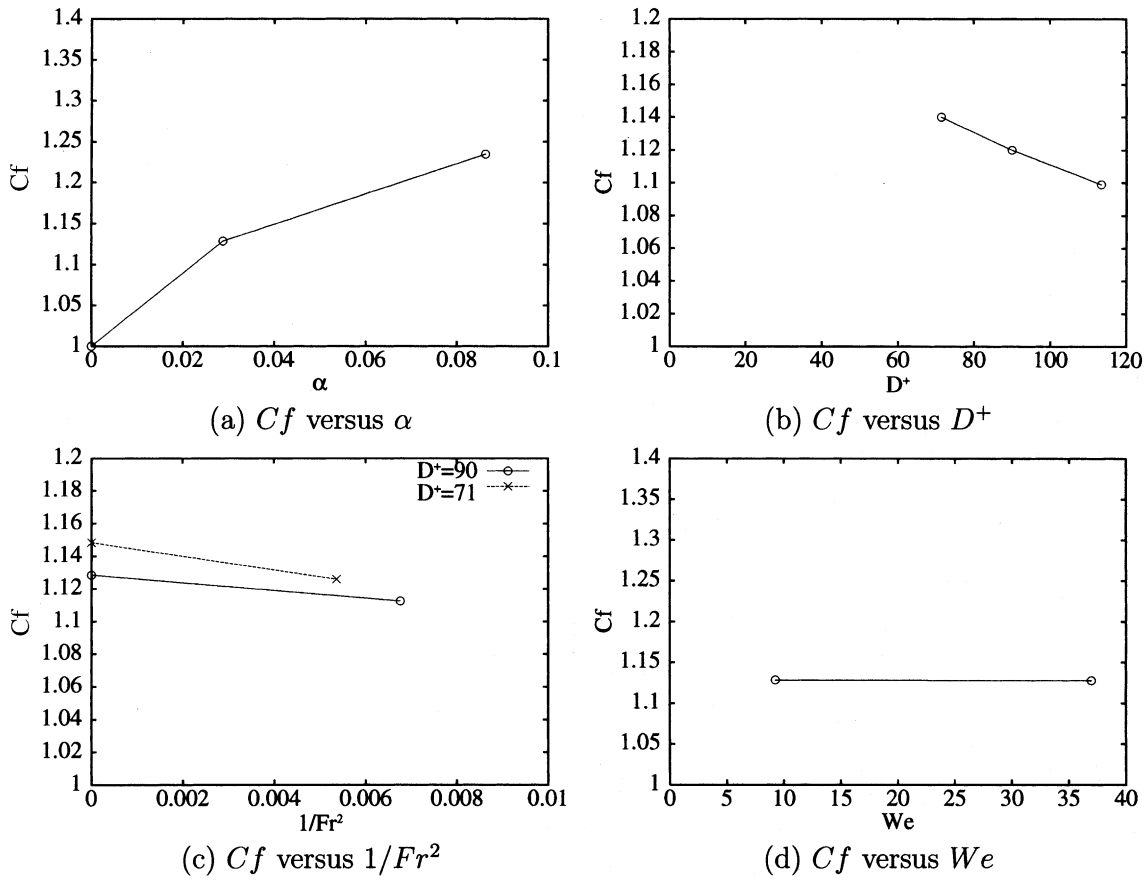

Fig. 14. Influence of α, D^+, Fr and We on the friction coefficient in the DNS of the bubbly channel flow.

DNS run-8, when the void ratio $\alpha = 8.6\%$. This qualitatively agrees with the measurement by Kato et al. (1999).

It is supposed that bubbles can influence the velocity fluctuation in two ways. One is the so-called "pseudo-turbulence", that is fluctuation of velocity signals due to passage of bubbles, and the second is modulation of liquid phase turbulence. The pseudo-turbulence is large when drift between the bubble and the liquid medium is present. The magnitude of the velocity fluctuation due to passage of bubbles is on the order of the drift velocity, and the fluctuation range over the distance of the order of the bubble diameter (Sugiyama et al., 2001). Even when drift between two phases is negligibly small like in the cases investigated in this study, interaction between bubbles and shear flow can cause pseudo-turbulence. It is assumed that the magnitude of the fluctuation is a function of the bubble diameter and the rate of shear, and that the distance which the fluctuation can reach is on the order of the thickness of the surface boundary layer around bubbles. These assumptions can explain that the increase in the wall-normal and spanwise intensities is larger at $D^+ = 71$ than at $D^+ = 113$ at the same void ratio of $\alpha = 2.9\%$. If the void ratio is kept constant, smaller bubble diameter means larger interfacial area and larger volume of the surface boundary layer in which velocity field is disturbed by the interaction between bubbles and shear flow. However, this pseudo-turbulence mechanism cannot explain the decrease in the streamwise component of the fluctuation, since the magnitude of the bubble-induced velocity in a shear flow is large in the direction of the flow. It is supposed that mechanisms other than this suppresses the streamwise fluctuation in the liquid phase turbulence.

5. Conclusions

A computational method for investigating the interactions between bubbles and turbulence has been developed in this study. The method employs a special front-tracking method, which tracks individual bubbles by the center positions and radius distributions. The advantage of the new method is that the interface curvature can be calculated more accurately for a given grid resolution. The accuracy validation carried out for a problem of single rising bubble has shown that the new method capable of accurate simulation of bubble dynamics with relatively small number of grid points.

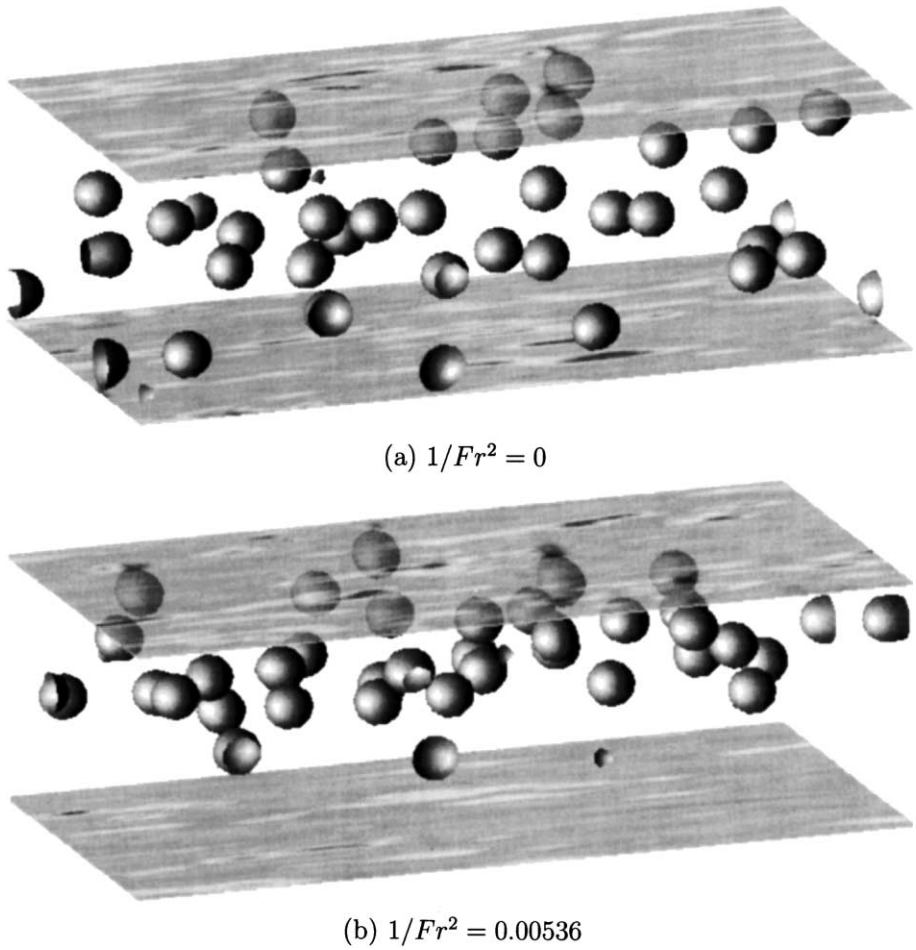

Fig. 15. Distribution of bubbles with or without gravity in the DNS of the bubbly channel flow. (a) $1/Fr^2 = 0$, (b) $1/Fr^2 = 0.00536$.

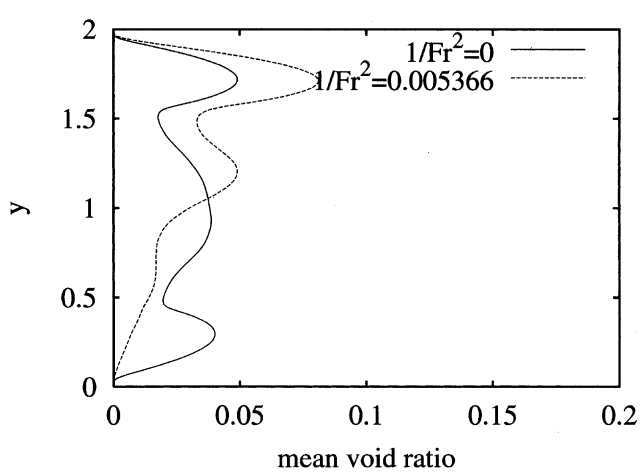

Fig. 16. Profiles of the time-averaged void ratio in the DNS of the bubbly channel flow.

This method was then applied to DNS computations of a low Reynolds number turbulent channel flow containing bubbles. The reduction of the frictional drag found in experiments were not confirmed in the present computations probably because of the low Reynolds number and the large bubble size relative to the channel width. On the other hand, the observed modification in the profiles of turbulence intensities were found to be in qualitative agreement with the experiment by Kato et al. (1999).

The validation of this numerical method applied to a turbulent flow is not yet sufficient. However, the preliminary computations in this study show that DNS of deforming bubbles in a low Reynolds number turbulent flow is feasible by use of the present numerical method. The number of grid points in one direction can be multiplied by eight with presently available computer resources by parallel processing. Considering the resolution required for resolving a bubble, the ratio of the bubble diameter to the channel half width (D/H) can be reduced to 0.05–0.1, which overlaps with the experimental conditions. The gap in the Reynolds number can be filled by introducing subgrid scale turbulence models. Since the present numerical method explicitly model the interactions between phases, it is expected

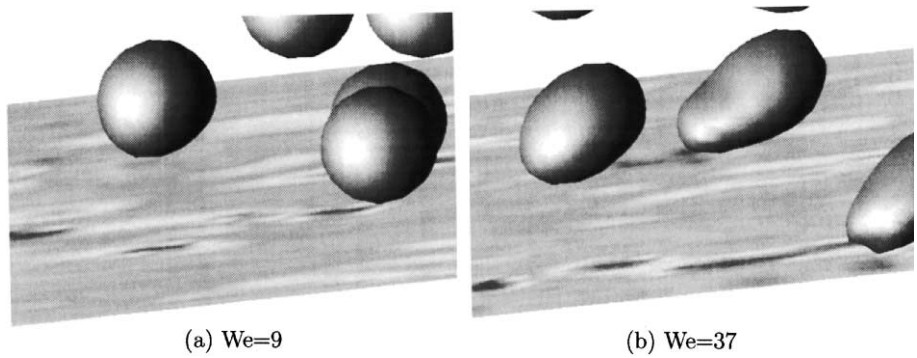

Fig. 17. Typical shape of bubbles near the wall in the DNS of the bubbly channel flow. (a) $We = 9$, (b) $We = 37$.

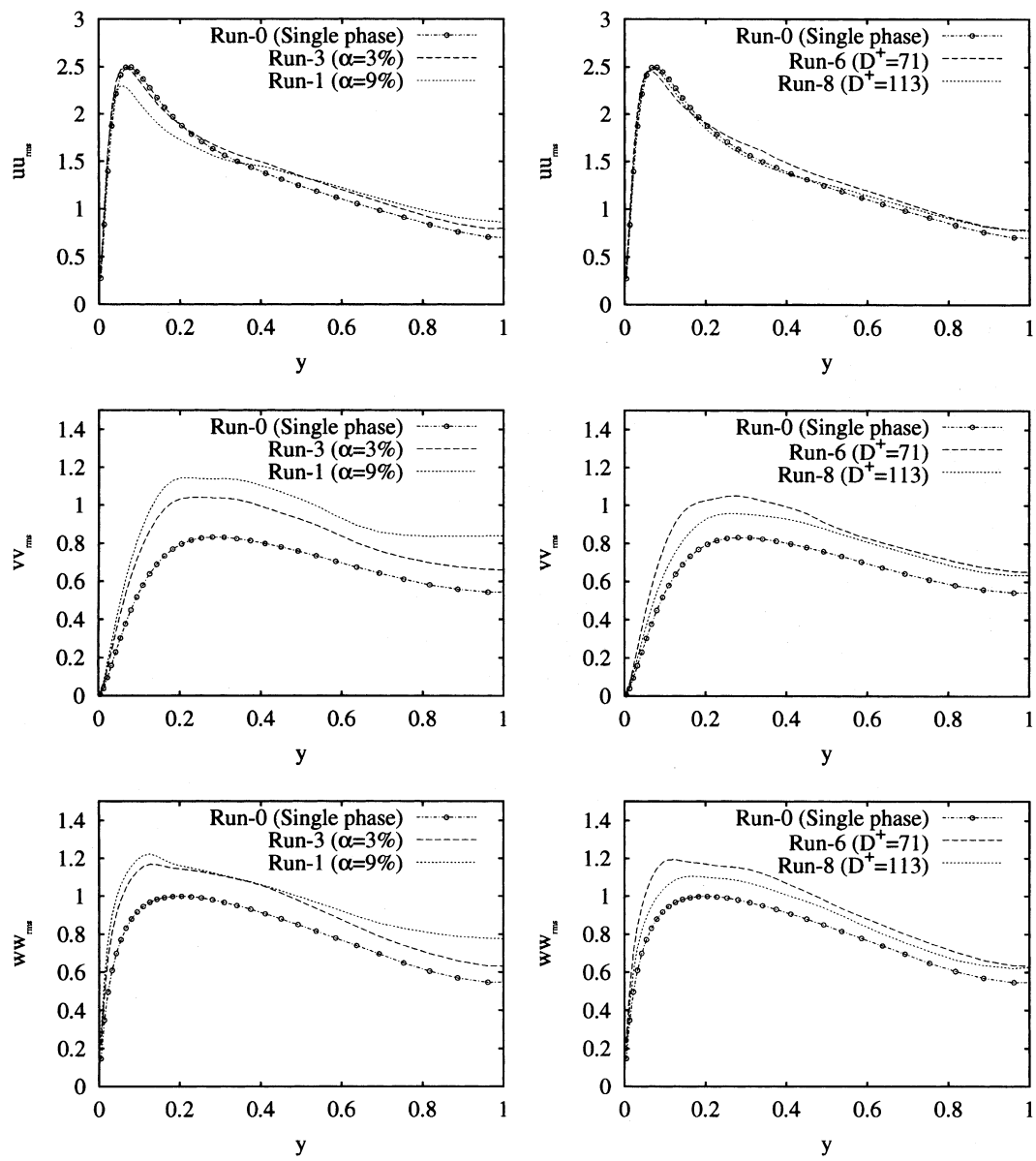

Fig. 18. Profiles of turbulence intensities in the DNS of the bubbly channel flow.

that subgrid scale models for single phase flows can be used for modeling small scale turbulence in the liquid phase.

References

Achenbach, E., 1974. Vortex shedding from spheres. Journal of Fluid Mechanics 62 (2), 209–221.

Drew, D.A., 1983. Mathematical modeling of two-phase flow. Annual Review of Fluid Mechanics 15, 261–291.

Ellingsen, K., Risso, F., 2001. On the rise of an ellipsoidal bubble in water: oscillatory paths and liquid-induced velocity. Journal of Fluid Mechanics 440, 235–268.

Elghobashi, S., Truesdell, G.C., 1992. Direct simulation of particle dispersion in a decaying isotropic turbulence. Journal of Fluid Mechanics 242, 655–700.

Gore, R.A., Crowe, C.T., 1989. Effect of particle size on modulating turbulent intensity. International Journal for Multiphase Flow 15 (2), 279–285.

Guin, M.M., Kato, H., Yamaguchi, H., 1996. Reduction of skin friction by microbubbles and its relation with near-wall bubble concentration in a channel. Journal of Marine Science and Technology 1, 241–254.

Hirt, C.W., Nichols, B.D., 1981. Volume of fluid (VOF) method for the dynamics of free boundaries. Journal of Computational Physics 39, 201–225.

Kajishima, T., Takiguchi, S., Hamasaki, H., 2001. Turbulence structure of particle-laden flow in a vertical plane channel due to vortex shedding. JSME International Journal Fluids and Thermal Engineering Series B 44 (4), 526–535.

Kanai, A., Miyata, H., 2001. Direct numerical simulation of wall turbulent flows with microbubbles. International Journal for Numerical Methods in Fluids 35, 593–615.

Kato, H., Iwashina, T., Miyanaga, M., Yamaguchi, H., 1999. Effect of microbubbles on the structure of turbulence in a turbulent boundary layer. Journal of Marine Science and Technology 4, 155–162.

Kim, J., Moin, P., Moser, R., 1986. Turbulence statistics in fully developed channel flow at low Reynolds number. Journal of Fluid Mechanics 177, 133–166.

Kubota, M., Akehata, T., Shirai, T., 1967. The behavior of single air bubbles in liquids of small viscosity. Chemical Engineering, Japan 31 (11), 1074–1080 (in Japanese).

Madavan, N.K, Deutsch, S., Merkle, C.L., 1985. Measurements of local skin friction in a microbubble-modified turbulent boundary layer. Journal of Fluid Mechanics 156, 237–256.

Osher, S., Sethian, J.A., 1998. Fronts propagating with curvature dependent speed: algorithm based on Hamilton–Jacobi formulation. Journal of Computational Physics 79, 12–49.

Ryskin, G., Leal, L.G., 1984. Numerical solution of free-boundary problems in fluid mechanics. Part 2. Buoyancy-driven motion of a gas bubble through a quiescent liquid. Journal of Fluid Mechanics 148, 19–35.

Sugiyama, K., Takagi, S., Matsumoto, Y., 2001. Multi-scale analysis of bubbly flows. Computer Methods in Applied Mechanics and Engineering 101, 689–704.

Takagi, S., Matsumoto, Y., 1995. Numerical study on the forces acting on a bubble and a particle. Proceedings of 3rd International Conference on Multiphase Flows, Lyon, France (CD-ROM).

Takahashi, T., Kakugawa, A., Kodama, Y., 1997. Streamwise distribution of the skin friction reduction by microbubbles. Journal of Society of Naval Architects of Japan 182, 1–8.

Takahashi, T., Kakugawa, A., Nagaya, S., Yanagihara, T., Kodama, S., 2001. Mechanisms and scale effects of skin friction reduction by microbubbles. Proceedings of the 2nd Symposium on Smart Control of Turbulence, Tokyo, Japan, pp. 79–87.

Takiguchi, S., Kajishima, T., Miyake, Y., 1998. Numerical Scheme to resolve the interaction between solid-particles and fluid-turbulence. Journal of the Japan Society of Mechanical Engineers B 64 (625), 2357–2364 (in Japanese).

Tomiyama, A., Kataoka, I., Sakaguchi, T., 1995. Drag coefficients of bubbles (1st report, Drag coefficients of a single bubble in a stagnant liquid). Journal of the Japan Society of Mechanical Engineers B 61 (587), 2357–2364 (in Japanese).

Unverdi, S.O., Tryggvason, G., 1992. A front-tracking method for viscous, incompressible, multi-fluid flows. Journal of Computational Physics 100, 25–37.